Soft Matter

Janus magnetoelastic membrane swimmers

Journal:	*Soft Matter*
Manuscript ID	SM-ART-06-2023-000788.R1
Article Type:	Paper
Date Submitted by the Author:	04-Aug-2023
Complete List of Authors:	Xiong, Yao; Northwestern University, Materials Science and Engineering Yuan, Hang; Northwestern University, Materials Science and Engineering Olvera de la Cruz, Monica; Northwestern University, Materials Science and Engineering

ARTICLE

Janus magnetoelastic membrane swimmers†

Yao Xiong,[a] Hang Yuan [b] and Monica Olvera de la Cruz *[acde]

Received 00th January 20xx,
Accepted 00th January 20xx

DOI: 10.1039/x0xx00000x

Soft swimming microrobots have attracted considerable attention due to their potential applications in diverse fields ranging from biomedicines to environmental remediation. The locomotion control is of importance to the research of micromachines and microrobots. Inspired by the motility strategies of living microorganisms, such as flagella, cilia, and euglenoids, we focus on propulsion mechanisms with a design of Janus magnetoelastic crystalline membrane microswimmers actuated by time-varying magnetic fields. Such a Janus swimmer consists of a ferromagnetic cap completed by a magnetoelastic membrane body, where superparamagnetic particles are uniformly distributed on the surface. Under the influence of external magnetic fields, the swimmer undergoes complex shape transitions due to the interplay between the magnetic dipole-dipole interactions, the elasticity of the magnetoelastic membranes, and also the hydrodynamics of surrounding fluids. We show that those shape changes are nonreciprocal, which can generate locomotion such that the propulsion speed can be optimized by tailoring the membrane elastic properties. Besides, we also demonstrate that the Janus swimmer can be magnetically guided in a spiral trajectory. With such adequate control locomotion in both speed and direction via non-invasive magnetic fields, this study provides another promising candidate design for the future development of microswimmers.

1. Introduction

Motile microorganisms, like cells and bacteria, can convert energy from their environment into motions in viscous fluids to conduct a series of biological processes.[1, 2] Inspired by the motility and sensing capabilities of living microorganisms, untethered biohybrid[3, 4] and artificial[5, 6] microswimmers have been developed and demonstrated their potentials in diverse fields ranging from biomedicines[7-10], target therapy[11-15], cargo transports[16, 17] to microswitches[18, 19], environmental remediation[20, 21], and pollutant degradation[22, 23]. In order to perform those specialized tasks, achieving controllable propulsion and navigation is of importance to the research of smart microswimmers.[24, 25] Over the past few decades, extensive efforts have been dedicated to endowing cell-scale swimmers with the capability of swimming.[26] Further advances in the strategies of designing programmable tactic behavior are highly desired to expand the use of microswimmers in complex environments.

Limited by the internal energy storage at the micrometer scale, microswimmers typically need power input from external energy sources to swim.[27] Energy delivery via magnetic fields has become a widely used method to actuate man-made tiny objects due to their intrinsic advantages in remote maneuverability, precise positioning capability, biocompatibility, and versatility.[27-32] Besides external energy, swimming at the microscopic level has additional requirements on the reciprocity of the movement. In the microscopic world, motions are usually dominated by viscous forces due to surrounding fluids, which is characterized by a low Reynolds number (*Re*)[22]. As explained by Purcell's Scallop Theorem[33], in low-*Re* regimes, the time reversibility and linearity of the Stokes equation elucidate that a microswimmer undergoing reciprocal movements simply goes back and forth and cannot produce net displacements. Low-*Re* swimming, therefore, requires nonreciprocal motions that possess at least two independent degrees of freedom and the prescribed variations in time sweep a finite area in the parameter space.[33-35] Hence, the strategies of designing magnetically driven microswimmers by introducing broken-symmetry often involve asymmetries in body shape or composite, creating flexible microstructures, introducing nonsymmetric environmental stimuli, and approaching boundaries.[28-30, 36-40]

Unlike traditional flagella/cilia type propulsion[2, 41], soft membranes can propel via body distortions like euglenids[42], vesicles[43], and synthetic lamellae[44-46]. Such irregular body deformations can also be realized by nonlinear elastic buckling of crystalline membranes under many conditions.[47-56] For example, deformable capsules under pressure changes adapt irregular morphologies[57-59]. Moreover, the self-assembled crystalline membranes, like the shells of viruses, generally buckle into shapes with icosahedral symmetry[60, 61]. Interestingly, diverse polyhedral shapes have been reported in membranes with build-in[62] or chemical-reaction-induced[63] heterogeneous elasticity. Recently, body deformations also have been

[a] Center for Computation & Theory of Soft Materials, Northwestern University, Evanston, IL, 60208, USA. E-mail: m-olvera@northwestern.edu
[b] Applied Physics Graduate Program, Northwestern University, Evanston, IL, 60208, USA
[c] Department of Materials Science and Engineering, Northwestern University, Evanston, IL, 60208, USA
[d] Department of Chemistry, Northwestern University, Evanston, IL, 60208, USA
[e] Department of Physics and Astronomy, Northwestern University, Evanston, IL, 60208, USA
†Electronic Supplementary Information (ESI) available. See DOI: 10.1039/x0xx00000x

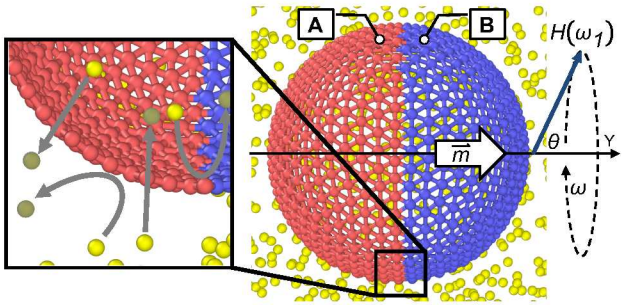

Fig. 1 Simulation setting of a Janus spherical shell suspending in a fluid. A small superparamagnetic particle is placed at each vertex of the hemisphere A (in pink). The hemisphere B (in blue) is presented as a rigid ferromagnetic cap with a permanent dipole, ***m***, which is perpendicular to the interface between the two hemispheres. The time-varying magnetic field, ***H***, is precessing around +*y*-direction with an angle θ. Zoom-in inset showing the possible routes of fluid particles (in yellow) after collisions with the shell.

accomplished in lipid vesicles by extruding the membrane with encapsulated bacteria[64, 65] or active particles[66, 67].

In this article, we computationally investigate the propulsion mechanism of Janus magnetoelastic crystalline membrane microswimmers that are actuated by a time-varying magnetic field. The Janus membrane shell is composed of a rigid ferromagnetic cap and a magnetoelastic crystalline membrane where superparamagnetic particles are uniformly distributed on the surface. We employ a coarse-grained membrane model for the Janus shell and adopt the dissipative particle dynamics (DPD) to account for the hydrodynamic interactions between the swimmer and the surrounding viscous fluid. We firstly explore the translational propulsion of the Janus shell in a uniaxial magnetic field and inspect the nonreciprocity of the morphology changes. Next, we optimize the propulsion speed by tailoring the mechanical properties of the magnetoelastic membrane and explain the mechanisms behind. Finally, we give an example that the Janus shell swims on a spiral path to demonstrate the feasibility of guiding the designed microswimmer in desired elaborated trajectories.

2. Method

In the present work, we investigate the morphological transitions and locomotion of Janus magnetoelastic crystalline membrane microswimmers. The Janus swimmer at room temperature is presented as a two-component spherical monolayer shell, which is penetrable and suspended in a viscous medium (Fig. 1). The hydrodynamic interactions between the Janus shell and fluids are introduced by employing a particle-based mesoscopic technique, called dissipative particle dynamics (DPD)[68-70].

2.1 Hydrodynamics: dissipative particle dynamics (DPD)

Here, we briefly introduce the DPD approach that we used to model the hydrodynamic effects due to the surrounding viscous fluid. More details of the DPD methodology can be found in the ref.[68-70]. The motion of DPD particles obeys the Newton's equations of motion: $d\mathbf{r}_i/dt = \mathbf{v}_i$, $d\mathbf{v}_i/dt = m\mathbf{f}_i$, where $\mathbf{r}_i$ and $\mathbf{v}_i$ are the position and the velocity of a particle i, respectively. For simplicity, the dimensionless mass of the DPD particles are set as $m = 1$ so that the total force acting on particle i, $\mathbf{f}_i$, is equal to its acceleration.[70] In general, this total force has three major contributions and is given by

$$\mathbf{f}_i = \sum_{j \neq i} \left(\mathbf{F}_{ij}^C + \mathbf{F}_{ij}^D + \mathbf{F}_{ij}^R\right). \quad (1)$$

The summation in the above equation takes over all particles j within a certain distance from particle i, i.e., the cut-off radius r_c. Explicitly, in eqn (1), the three forces[68-70] acting on particle i by particle j are the purely repulsive conservative force $\mathbf{F}_{ij}^C = a_{ij}\left(1 - r_{ij}/r_c\right)\hat{\mathbf{r}}_{ij}$, the dissipative force $\mathbf{F}_{ij}^D = -\gamma\omega^D\left(r_{ij}\right)\left(\hat{\mathbf{r}}_{ij} \cdot \mathbf{v}_{ij}\right)\hat{\mathbf{r}}_{ij}$, and the random force $\mathbf{F}_{ij}^R = \sigma\omega^R\left(r_{ij}\right)\theta_{ij}\hat{\mathbf{r}}_{ij}$, respectively. The coefficient a_{ij} represents the maximum repulsion between particles. $r_{ij} = |\mathbf{r}_{ij}|$ is the distance between the centers of these two particles, $\mathbf{r}_{ij} = \mathbf{r}_i - \mathbf{r}_j$, and $\hat{\mathbf{r}}_{ij} = \mathbf{r}_{ij}/r_{ij}$. γ and σ are the strengths of the dissipative and random forces, and $\mathbf{v}_{ij} = \mathbf{v}_i - \mathbf{v}_j$ is the relative particle velocity. $\omega^D\left(r_{ij}\right)$ and $\omega^R\left(r_{ij}\right)$ are two weight functions. The θ_{ij} is a randomly fluctuating variable with Gaussian statistics: $\langle\theta_{ij}(t)\rangle = 0$ and $\langle\theta_{ij}(t)\theta_{ij}(t')\rangle = (\delta_{ik}\delta_{jl} + \delta_{il}\delta_{jk})\delta(t - t')$, where δ_{ij} is the Kronecker delta in practice. The cut-off radius, beyond which all the three additive components of $\mathbf{f}_i$ vanish, defines the characteristic length scale of the system. The dissipative force, $\mathbf{F}_{ij}^D$, dampens the effects of the random force, $\mathbf{F}_{ij}^R$, which accounts for the Brownian motion. These two forces together form the thermostat as the Brownian dashpot, which is a minimal model representing viscous forces and thermal noise between the DPD particles.[71, 72] For a near-equilibrium system, these two forces are related via the fluctuation-dissipation theorem (FDT), which is fulfilled by imposing the following two conditions: $\omega^D\left(r_{ij}\right) = \left(\omega^R\left(r_{ij}\right)\right)^2$, and $\sigma^2 = 2\gamma\epsilon$, where ϵ is the characteristic energy scale. As a simple choice, the weight functions are taken as $\left(\omega^R\left(r_{ij}\right)\right)^2 = \left(1 - r_{ij}/r_c\right)^2$ for $r_{ij} < r_c$, and zero otherwise.

In the context of DPD, a modified version of the velocity-Verlet algorithm[70] is used to advance the set of positions and velocities. In this study, the DPD simulations use reduced units for length, mass, energy, time as $r_c = m = \epsilon = 1$. The corresponding physical units will be provided in section 2.3. We use the DPD module as implemented in the LAMMPS simulation package[73, 74] to integrate the equations of motion. All simulation snapshots are visualized using the Open Visualization Tool (OVITO)[75]. The fluid particles are omitted for clarity in figures shown in this article.

2.2 Membrane model

A shell can be triangulated to a lattice structure with at least twelve isolated 5-fold disclinations as the protocol introduced by Caspar and Klug[76]. Such a lattice is characterized by a pair of integers, (p, q), which defines the total number of lattice sites by $N = 10(p^2 + pq + q^2) + 2$. In this study, different choices of (p, q) are probed and do not affect primary results presented in this

work. Here, we select (6, 6) to perform all simulations, which results in $N = 1082$ linked vertices, 3240 edges, and 2160 triangular faces. In our simulations, the shell is modeled by 1082 bonded DPD particles that are initially placed at each vertex of triangulation (Fig. 1). These shell particles are equally grouped into two sets, i.e., $\mathbf{P}_\mathrm{A}$ for particles on hemisphere A (in pink) and $\mathbf{P}_\mathrm{B}$ for particles on hemisphere B (in blue), to be imparted different mechanical and magnetic properties as detailed latter.

According to the discretization scheme of the continuum expression for the elastic energy proposed by Nelson *et al.* [61, 77], the elastic component of the Hamiltonian of a thin shell, H_e, has contributions from stretching, H_s, and bending, H_b. In our simulations, the stretching and bending of shells are modeled by harmonic bond and harmonic dihedral interactions, respectively, and the corresponding energies are calculated by

$$H_s = \sum_{e\in\mathbf{E}} \frac{k_{ij}}{2}\left(\left|\mathbf{r}_i^e - \mathbf{r}_j^e\right| - r_0\right)^2, \tag{2}$$

and

$$H_b = \sum_{e\in\mathbf{E}} \frac{\tilde{\kappa}_{kl}}{2}|\mathbf{n}_k^e - \mathbf{n}_l^e|^2 = \sum_{e\in\mathbf{E}} \tilde{\kappa}_{kl}(1-\cos\phi_{kl}). \tag{3}$$

The summations on the right-hand-side of eqn (2) and (3) run over all e elements of the set of all bonds, $\mathbf{E}$. A bond e connects particles i and j, and has an equilibrium length of r_0. k_{ij} is the microscopic stretching constant, sometimes referred to as the spring constant or bond strength, of the bond e. $\mathbf{r}_i^e$ and $\mathbf{r}_j^e$ are the position vectors of the two particles connected by the bond e. The coefficient $\tilde{\kappa}_{kl}$ is the microscopic bending rigidity along the bond e shared by triangles k and l whose normal vectors are $\mathbf{n}_k^e$ and $\mathbf{n}_l^e$, and $\cos\phi_{kl}$ is the dihedral angle of the two triangles. To determine the elastic properties at the interface between the two components, following the ref.[78], we select the value of k_{ij} based on the rule of springs occurring in series, ${k_{ij}}^{-1} = {k_i}^{-1} + {k_j}^{-1}$, or explicitly, $k_{AA} = k_A/2$, $k_{BB} = k_B/2$, and $k_{AB} = k_{BA} = k_A k_B/(k_A k_B)$, where k_A and k_B are the microscopic stretching constant (or referred to as bond strength) assigned for particle $i \in \mathbf{P}_\mathrm{A}$ and particle $i \in \mathbf{P}_\mathrm{B}$, respectively. Similarly, the value of the microscopic bending rigidity is chosen based on the type of the four particles comprising the dihedral: $\tilde{\kappa}_{AA} = \tilde{\kappa}_A$ for all four particles belonging to $\mathbf{P}_\mathrm{A}$, $\tilde{\kappa}_{BB} = \tilde{\kappa}_B$ for all four particles belonging to $\mathbf{P}_\mathrm{B}$, and $\tilde{\kappa}_{AB} = \tilde{\kappa}_{BA} = (\tilde{\kappa}_A + \tilde{\kappa}_B)/2$ for mixed types.

In our study, the hemisphere A (in pink, Fig 1) is modeled as a magnetoelastic membrane by placing a small superparamagnetic particle at the center of each particle $i \in \mathbf{P}_\mathrm{A}$. An external magnetic field induces a magnetic dipole on each particle $i \in \mathbf{P}_\mathrm{A}$. The induced magnetic dipoles are supposed to be identical and always oriented in the direction of the field. We can write the additional energy contribution accounting for magnetic dipole-dipole interactions as

$$H_m = -\frac{\mu_0}{4\pi}\sum_{i,j\in\mathbf{P}_\mathrm{A}, i\neq j} \frac{1}{{r_{ij}}^3}\left[3\left(\boldsymbol{\mu}\cdot\hat{\mathbf{r}}_{ij}\right)^2 - \boldsymbol{\mu}^2\right], \tag{4}$$

where μ_0 and $\boldsymbol{\mu}$ are the magnetic permeability in vacuum and the induced magnetic dipole moment of particle $i \in \mathbf{P}_\mathrm{A}$. In the linear regime, the magnetic dipole moment is correlated with the external magnetic field, $\boldsymbol{H}$, as

$$\boldsymbol{\mu} = \frac{\pi}{6} d^3 \chi \boldsymbol{H}, \tag{5}$$

where d and χ are the diameter and magnetic susceptibility of the superparamagnetic particles (SPs), respectively. In our simulations, we model the uniform magnetic fields implicitly by constraining the orientation of the dipole moment of all particles $i \in \mathbf{P}_\mathrm{A}$ in the same direction as the field, i.e.

$$\boldsymbol{\mu} = \mu\hat{\boldsymbol{\mu}}, \tag{6}$$

where $\hat{\boldsymbol{\mu}}$ represent the direction of the dipole moment of the SPs as well as that of the external magnetic field. The coefficient μ characterizes the strength of the induced dipoles.

Using the rigid body package in LAMMPS, the hemisphere B (in blue, Fig. 1) is modeled as a rigid ferromagnetic cap (FC). The total force and torque acting on the cap are computed as the sum of the forces and torques on each particle $i \in \mathbf{P}_\mathrm{B}$. Then, the coordinates and velocities of the constituent particles are updated so that the cap moves and rotates as a single entity. The FC has a permanent magnetic dipole moment, $\boldsymbol{m}$, that is perpendicular to the interface between hemispheres A and B (Fig. 1). In a magnetic field $\boldsymbol{H}$, any misalignment of the cap's permanent dipole with the field will contribute extra energy as $H_{fm} = -\boldsymbol{m}\cdot\boldsymbol{H}$, and result in an additional magnetic torque[79] on the cap according to $\boldsymbol{T}_\mathrm{fm} = \mu_0\boldsymbol{m}\times\boldsymbol{H}$. Substituting with eqn (5) and (6), this magnetic torque is given by

$$\boldsymbol{T}_\mathrm{fm} = \frac{6\mu_0\mu}{\pi d^3\chi}\boldsymbol{m}\times\hat{\boldsymbol{\mu}}. \tag{7}$$

For simplicity, we neglect the magnetic interactions of particle $i \in \mathbf{P}_\mathrm{A}$ with particle $i \in \mathbf{P}_\mathrm{B}$. According to eqn (7), we know $T_\mathrm{fm} \propto |\boldsymbol{m}\times\hat{\boldsymbol{\mu}}|$ and this magnetic torque due to FC can be rewritten as

$$\boldsymbol{T}_\mathrm{fm} = k_\mathrm{fm}\hat{\boldsymbol{m}}\times\hat{\boldsymbol{\mu}}, \tag{8}$$

where k_fm is a coefficient that characterizes the strength of the magnetic torque and depends on the strength of the magnetic dipoles of the SPs. $\hat{\boldsymbol{m}}$ stands for the unit vector of the permanent dipole moment of the cap, which also is used to define the orientation of our Janus shells. For simplification, k_fm is set to a large enough value so that the shell is oriented in the direction of the field. The magnetic torque on hemisphere B is exerted using the add torque package in LAMMPS.

2.3 DPD Simulation setup and physical units

We choose the number density of DPD particles as $\rho = 3\,{r_c}^{-3}$. As mentioned above, our DPD simulations use reduced units for length, mass, energy as $r_c = m = \epsilon = 1$. We can map those DPD reduced units onto the corresponding physical units, which is summarized in Table 1. Setting the length unit as $l_0 = 1$ μm, the unit of mass that corresponds to liquid water is $m_0 = 3.33\times10^{-16}$ kg. We fix the energy unit as $k^BT = 4.14\times10^{-21}$ J in all simulations, where k^B is the Boltzmann constant and the temperature is $T = 300$ K. The time scale is then derived

Table 1 Characteristic quantities.

Physical quantities	Characteristic quantities	Values
Length (r_c)	l_0	1.0 μm
Mass (m)	m_0	3.33×10^{-16} kg
Energy (ϵ)	k^BT	4.14×10^{-21} J
Time (τ)	$\tau_0 = l_0\sqrt{m_0/k^BT}$	2.84×10^{-4} s

as $\tau_0 = l_0\sqrt{m_0/k^BT} = 2.84 \times 10^{-4}$ s . To match the compressibility of water for a DPD system, the repulsion parameter is chosen to be $a = 75/\rho$ in units of ϵ/r_c.[70] Here, we set the repulsion parameter $a_{ij} = 25$ for all particle pairs in order to exclude other effects other than hydrodynamic interactions between the shell and fluids. The strength of the random forces is chosen as $\sigma = 3$ in units of $\left(\sqrt{m\epsilon}/r_c\right)^{1/2}$. Correspondingly, we have $\gamma = 4.5$ in units of $\sqrt{m\epsilon}/r_c$. The timestep is $\Delta t = 0.001\,\tau$.

For all simulations, the box is $40\,r_c \times 40\,r_c \times 40\,r_c$ in size and periodic boundary conditions are applied in all directions. The initial radius of spherical shells is $5\,r_c$ (corresponding to 5 μm), where the equilibrium bond length is $r_{\text{eq}} = 0.58\,r_c$. We select the following parameters for our reference sample (denoted as sample S1), including $k_A = 900\ \epsilon/{r_c}^2$, $k_B = 3000\ \epsilon/{r_c}^2$, $\tilde{\kappa}_A = 50\,\epsilon$, and $\tilde{\kappa}_B = 50\,\epsilon$. It should be noticed that the hemisphere B is modeled as a rigid body and the choices of k_B and $\tilde{\kappa}_B$ only affect the mechanical properties of the interface linking the two hemispheres. Hence, a sufficiently large value of k_B renders a strong interface and ensures the integrity of the Janus shell structure. The relative importance of stretching versus bending in morphology transitions of soft elastic membranes can be quantitatively characterized by a dimensionless quantity called the Föppl-von Kármán (FvK) number[61, 77, 80],

$$\gamma = \frac{YR^2}{\kappa}. \tag{9}$$

In the continuum limit[77, 81], $Y = 2k/\sqrt{3}$ is the 2D Young's modulus for a hexagonal array of bonded particles and has units of energy per area, and $\kappa = \sqrt{3}\tilde{\kappa}/2$ is the bending rigidity. Correspondingly, the FvK number of the magnetoelastic membrane (hemisphere A) with reference parameters is $\gamma = 600$.

Initially, the spherical Janus shell of 1082 bonded particles (equally grouped to set $\mathbf{P}_\text{A}$ and $\mathbf{P}_\text{B}$) is immersed in randomly created fluid particles. The shell is constructed to have an orientation, defined by the permanent dipole $\boldsymbol{m}$, in the +*y*-direction. We probed different values of the equilibration bond length r_0 and find that reducing r_0 smaller than r_{eq} results in a faster recovery process and less spinning when the external magnetic field cannot provide sufficient magnetic torques on the FC to restrain the random rotation. Hence, an equilibration procedure is executed prior to all production simulations: the equilibration bond length is rescaled as $r_0 = 0.7r_{\text{eq}} = 0.41\,r_c$, and then the shell is equilibrating for 5×10^3 simulation timesteps with no external magnetic fields.

At the beginning of production runs, uniform and implicit external fields are introduced by identically assigning the dipole moment $\boldsymbol{\mu}$ of the SPs in each particle $i \in \mathbf{P}_\text{A}$ (eqn (6)). The dipole moment has units of $\sqrt{4\pi {r_c}^3\epsilon/\mu_0}$ in DPD simulations. Assuming each vertex/particle represents a 10 nm superparamagnetic particle, the magnitude of the dipole moment represents typical values (20~140 $\text{A}\cdot\text{m}^2/\text{kg}$)[82]. As shown in Fig. 1, the instantaneous dipole orientation due to a magnetic field precessing around +*y*-direction is given by

$$\hat{\boldsymbol{\mu}} = \sin\theta\sin\omega t\ \hat{\boldsymbol{\imath}} + \cos\theta\,\hat{\boldsymbol{\jmath}} + \sin\theta\cos\omega t\,\hat{\boldsymbol{k}}, \tag{10}$$

where θ is the precession angle and ω is the precession frequency in units of τ^{-1}. We remain $\omega = 0.5\,\tau^{-1}$ ($\sim 1760\ \text{s}^{-1}$), and all production simulations run at least 1.7×10^6 timesteps ($1.7 \times 10^3\,\tau$). Similar to the FvK number, the relative strength between magnetic energy and bending energy can be characterized by a dimensionless quantity called magnetoelastic parameter[56, 83],

$$\Gamma = \frac{MR^2}{\kappa}, \tag{11}$$

where $M = 8\sqrt{3}\widetilde{M}/{r_\text{eq}}^2$ is the magnetic modulus defined in the continuum limit and $\widetilde{M} = (1/4)(\mu_0/4\pi)\left(9\mu^2/{r_\text{eq}}^3\right)(2/3)$. The magnetoelastic parameter of the magnetoelastic membrane with reference parameters is $\Gamma = 336$ when the strength of the induced magnetic dipole is $\mu = 1.36$ in units of $\sqrt{4\pi {r_c}^3\epsilon/\mu_0}$.

3. Results and discussion

Recall that a nonreciprocal motion[33, 34], sometimes referred to as time-irreversible motion, is required for microswimmers to swim at a low Reynolds number (Re). In our work, we employ a "breaking-symmetry" strategy using Janus membrane shells that are actuated and navigated by external magnetic fields. The uniform field that has a time-varying intensity and is precessing around +*y*-direction at a frequency of ω (Fig. 1). In our simulations, the magnetic field is modeled implicitly by constraining the magnetic dipole moment of superparamagnetic particles (SPs) on hemisphere A, $\boldsymbol{\mu}$, as detailed in Section 2.2.

3.1 Translational propulsion in uniaxial magnetic field

In our first series of simulations, the Janus shell with reference parameters (denoted as S1: $k_A = 900\ \epsilon/{r_c}^2$, $k_B = 3000\ \epsilon/{r_c}^2$, $\tilde{\kappa}_A = 50\,\epsilon$, and $\tilde{\kappa}_B = 50\,\epsilon$) is subjected to an uniaxial magnetic field, i.e. the precession angle $\theta = 0°$. To obtain a nonzero net displacement in the desired direction, +*y*-direction, we select the magnetic field having zero magnitude in -*y*-direction to avoid that the Janus shell is periodically flipped due to the magnetic torque on the ferromagnetic cap (FC, hemisphere B, Fig. 1). Here, the instantaneous magnetic dipole moment of the SPs, which has the same direction as the magnetic field, is given by $\boldsymbol{\mu} = \mu(t)\,\hat{\boldsymbol{\jmath}}$, where $\mu(t) = 1.36\sin\omega_1 t$, for $2n\pi \le \omega_1 t \le (2n+1)\pi$ (where $n = 0,1,2,\ldots$), and zero otherwise. Here, we select $\omega_1 = 0.5\,\tau^{-1}$ ($\sim 1760\ \text{s}^{-1}$). As illustrated in Fig. 2A, the dipole moment of the SPs exhibits a profile of half-wave-rectified sine waves in its intensity: the

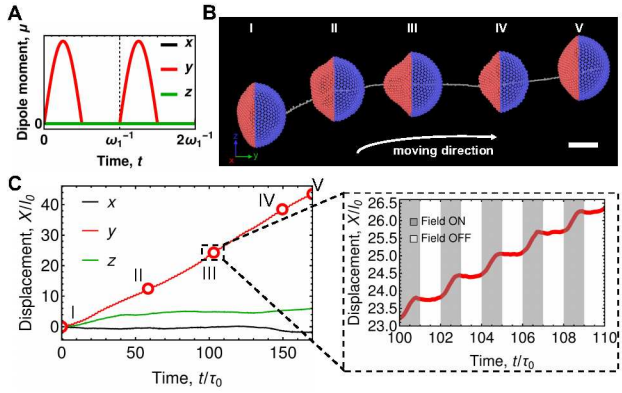

Fig. 2 Propulsion of the Janus shell in the uniaxial magnetic field. (A) Scheme of the time evolution of the induced dipole moment within two periods. (B) Snapshots of the shell at five selected timesteps as I~V marked in (C). The gray line represents the trajectory of the center of mass of the hemisphere B. The scale bar is 5 μm. (C) Time evolution of displacements.

magnitude of the dipole moment along $+y$-direction increases sinusoidally before it attenuates to zero during the first half of the period and remains zero during the second half.

Our simulation shows that the swimmer propels primarily along $+y$-direction with cyclical configuration changes in the hemisphere A (Fig. 2B). The corresponding time evolution of displacements along all three directions are presented in Fig. 2C. Comparing with the dominant displacement in $+y$-direction, the components in x- and z-directions are small but visible, which are attributed to the random spinning of the shell when the field cannot provide sufficient magnetic torques on the ferromagnetic cap. As shown in the inset of Fig. 2C, we also observe a forward stroke as the magnetic field ramps up, followed by a backward stroke when the field is decreasing and off. Comparing with the backward stroke of each period, the forward stroke produces a larger displacement, leading to a net forward propulsion.

To inspect the physics governing the propulsion observed in our simulations, we focus on the dynamics of the shell within one period and quantitatively characterize the deviation of the shell shape from a perfect sphere through the asphericity [61]:

$$b = \frac{\langle \Delta R^2 \rangle}{\langle R \rangle^2} = \frac{1}{N_v} \sum_{i=1}^{N_v} \frac{(R_i - \langle R \rangle)^2}{\langle R \rangle^2}, \qquad (12)$$

where R_i is the radial distance of particle i from the center of mass of the shell and $\langle R \rangle$ is the mean radius,

$$\langle R \rangle = \frac{1}{N} \sum_{i=1}^{N_v} R_i . \qquad (13)$$

Specifically, we also calculate the volume enclosed by the penetrable shell through

$$V = \sum_k \Omega_k , \qquad (14)$$

where $\Omega_k = \mathbf{r}_{k,1} \cdot \mathbf{r}_{k,2} \times \mathbf{r}_{k,3}/6$ is the signed volume of the tetrahedron extended by the triangle k on the membrane consisting of three clockwise-ordered vertices: $\mathbf{r}_{k,1}$, $\mathbf{r}_{k,2}$, $\mathbf{r}_{k,3}$.

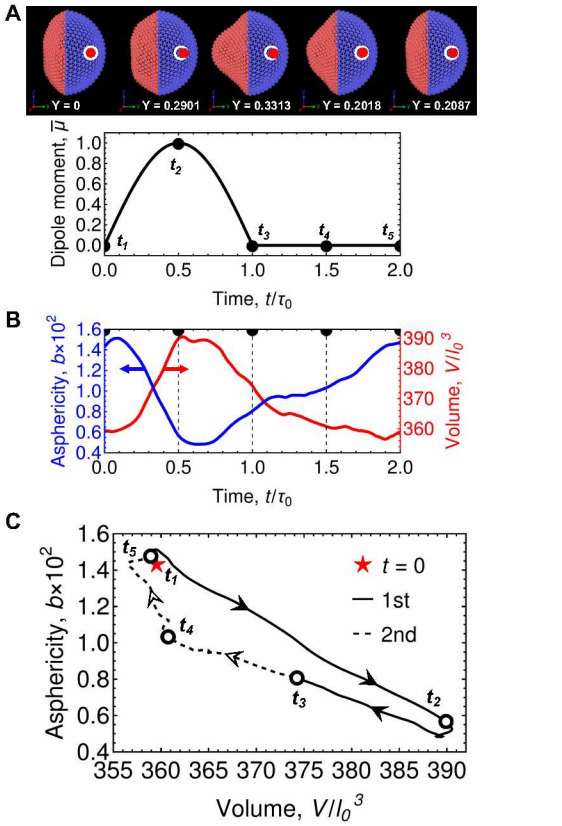

Fig. 3 Nonreciprocal dynamics of the Janus shell in one period of the uniaxial magnetic field. (A) Snapshots of the Janus shell at five selected moments, t_1~t_5 (from left to right, as marked in the time evolution of the normalized dipole moment strength, $\bar{\mu}$). The white open circles and red dots represent the location of the center of mass of hemisphere B at the beginning and each corresponding frame, respectively. The number below each snapshot is the relative displacement in y-direction. (B) Time evolutions of asphericity, b (in blue, left axis) and volume (in red, right axis). (C) The asphericity-volume (b-V) parameter space. The red star presents the beginning of the period and arrows point out the time direction. The paths of first and second halves are indicated by the solid and dashed lines, respectively.

Fig. 3A shows snapshots at five selected moments t_1~t_5 as marked in the time evolution of the normalized dipole moment, $\bar{\mu} = \mu/1.36$. We also mark the positions of the center of mass of hemisphere B at the initial frame and each selected moment by the white open circle and red points, respectively. The relative position of the two markers implies that the shell goes forth during the first half ($t_1 \rightarrow t_3$) and back during the latter half ($t_3 \rightarrow t_5$). In Fig. 3B, we plot the time evolutions of the asphericity b (in blue, left axis) and the volume V (in red, right axis). In response to the increasing external field ($t_1 \rightarrow t_2$), the hemisphere A (in pink) bulges out with a roughly flat tip, corresponding to a decrease in the asphericity b and an increase in the volume V. The recession ($t_2 \rightarrow t_3$) and removal of the field ($t_3 \rightarrow t_5$) cause the hemisphere A to slowly expel fluids from the inside and contract with a rounded top, and the shell eventually

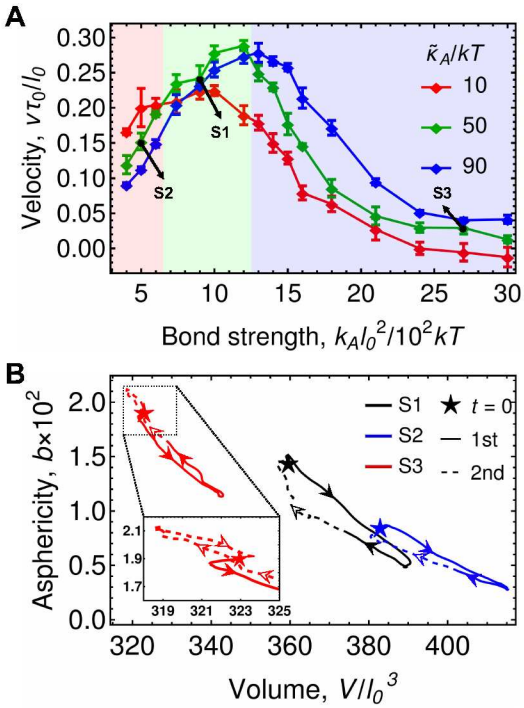

Fig. 4 Effects of mechanical properties on propelling velocity in the uniaxial magnetic field. (A) Swimming velocity as a function of bond strength k_A. Each data point stands for three independent simulation runs. (B) The asphericity-volume (b-V) parameter space. The parameters of the three samples, S1, S2, and S3, are marked in (A). Data are taken from one representative period of each sample. The open circles present the beginning of the period and arrows point out the time direction. The paths of first and second halves are indicated by the solid and dashed lines, respectively.

recovers back to the shape as at the beginning of the cycle. Comparing with the swelling phase ($t_1 \rightarrow t_2$), the recovery phase ($t_2 \rightarrow t_5$) happens significantly slower. In the ($b-V$) parameter space, we also observe a closed loop swept by the corresponding variations in time (Fig. 3C). It confirms that the microswimmer swims along a time-irreversible path, namely, a nonreciprocal motion. Our results indicate that the nonsymmetric magnetic field results in the mismatch in time scales associated with the swelling and deswelling processes and yields a nonreciprocal motion that promises such a Janus shell to periodically propel forward at low *Re*.

3.2 Effects of elasticity of the magnetoelastic membrane

We also investigate the effects of mechanical properties of the magnetoelastic membrane (hemisphere A) on the propelling velocity in the uniaxial magnetic field. Here, we fix the parameters of hemisphere B as $k_B = 3000\ \epsilon/{r_c}^2$ and $\tilde{\kappa}_B = 50\ \epsilon$, and vary k_A in the range of 400~3000 $\epsilon/{r_c}^2$ by choosing $\tilde{\kappa}_A$ from 10, 50, and 90 ϵ. The propelling velocity is defined as the time average of displacement in each entire simulation. As summarized in Fig. 4A, the dependence of propelling velocity on the microscopic spring constant, k_A, is not monotonic for all three microscopic bending rigidities $\tilde{\kappa}_A$. Each data point in Fig. 4A stands for the average over three independent simulations runs and the error bar corresponds to the standard deviation. At a given $\tilde{\kappa}_A$, the velocity decreases if the bond strength k_A is either too small or too large and exhibits a maximum velocity at an optimal value, $k_{A,m}$.

To understand the trend of propelling velocity observed above, as marked in Fig. 4A, we pick up another two swimmers of $\tilde{\kappa}_A = 50\ \epsilon$ along with the reference sample (sample S1), including $k_A = 500$ (sample S2) and 2700 $\epsilon/{r_c}^2$ (sample S3), and demonstrate the time evolutions in one representative period of sample S1~S3 with respect to the asphericity b (Fig. S1A), the volume V (Fig. S1B), and the displacement in y-direction (Fig. S1C) in the Supplementary Information (ESI†). At a given microscopic bending rigidity $\tilde{\kappa}_A$ increasing the microscopic spring constant k_A results in the asphericity shifting to higher values and the volume dropping to lower values. Our results show that the respective fluctuating amplitude of asphericity and volume occurs in similar ranges for the three samples, including $\Delta b \approx 0.008$ and $\Delta V \approx 20\ {r_c}^3$. In other words, increasing the Young's modulus of the magnetoelastic membrane (hemisphere A) does not affect the amount of fluids absorbed or expelled, but drives the shell to a less spherical shape. As shown in Fig. S1C of ESI†, all three samples exhibit forward and backward strokes in one cycle. The forward stroke generated by increasing the dipole moment strength of the SPs produces the largest displacement in sample S1 ($k_A = 900\ \epsilon/{r_c}^2$), followed by sample S2 ($k_A = 500\ \epsilon/{r_c}^2$) and then sample S3 ($k_A = 2700\ \epsilon/{r_c}^2$). All three samples continue swimming for finite distances after the field begins attenuating, and then the sample with the highest Young's modulus, sample S3, swims backward first. Comparing with sample S1, other two samples propel backward substantially prior to moving forward again during the second half.

We first inspect the propulsion mechanism in rigid case (sample S2) and then the soft case (sample S3). In Fig. 4B, we plot the variations in time in the asphericity-volume (b-V) parameter space where the solid and hollow arrows imply the direction of time. We also add the data of sample S1 shown in Fig. 3C to Fig. 4B for comparison, and all three samples exhibit closed loops in the (b-V) parameter space. We find that the larger the area of the closed loop in the parameter space, the faster the Janus shell propels: the circle of sample S1 which move fastest among the three samples has the largest area, while sample S3 moving slowest occupies the smallest circle. A similar trend is also reported in bilayer vesicles[43] where the swimming velocity roughly scales as the square-root of the area enclosed by loops in the parameter space. A smaller cycle in the asphericity-volume (b-V) parameter space indicates a stronger correlation between the two characteristic parameters, which reduces the system's degree of freedom. Hence, at a given $\tilde{\kappa}_A$ the motion trends to be reciprocal for relatively rigid magnetoelastic membranes (higher k_A). We also plot the forward, backward, and net displacements of one period averaged over all cycles of individual simulation (see Fig. S2 in ESI†). As schemed in Fig. S1C of ESI†, a forward displacement, X_f, is defined as the maximum displacement during the first half of the period, and a

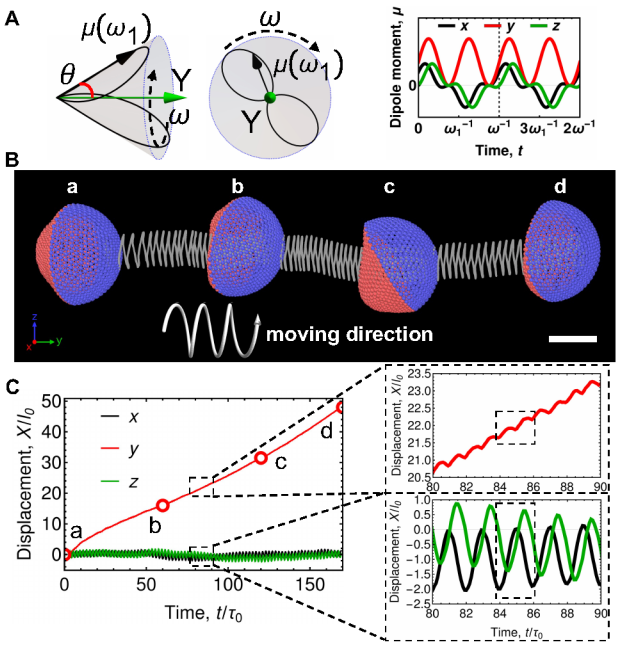

Fig. 5 Motion of the Janus shell in the precessing magnetic field. (A) Schemes of side view (left), front view (middle) of the precessing field with a varying intensity, and the time evolution of the induced dipole moment within two periods (right). (B) Magnetic guidance of the Janus shell with a spiral trajectory. The gray line going through the shell is the trajectory of the center of mass of the hemisphere B. The white arrow below the snapshots schematically shows the spiral movement. The scale bar is 5 μm. (C) Time evolution of displacements. One period is highlighted by dashed box in the inset.

backward displacement, X_b, is computed as the difference of the net displacement X_n with X_f. Our results show that the Janus shells with high values of k_A periodically swims back and forth with approximate distance but in the opposite direction, leading to roughly staying in the same spot after periods.

We next examine the propulsion of Janus shells with smaller k_A. Recall that the morphology transition of closed magnetoelastic membranes is a result of the competition between the elasticity and the magnetic dipole-dipole interactions.[56] In our study, passive fluid particles are able to penetrate the magnetoelastic membrane of hemisphere A from both inside and outside, triggering the changes in the volume enclosed by the shell. Hence, the morphology transition of our penetrable Janus swimmers becomes a result of the interplay of the elasticity with the magnetic dipole-dipole interactions as well as the hydrodynamic interactions. It has been shown that the jet propulsion velocity of a swimmer with fixed body shape is inversely proportional to both the swimmer's longitudinal and transverse dimensions at low Re.[84] As shown in Fig. S1B of ESI†, the shell with a relatively soft hemisphere A often possesses a larger volume and, correspondingly, a larger size along the y-direction. Hence, stronger drag forces applied on the hemisphere A that generate slower propulsion are anticipated as one is approaching the lower limit of k_A.

We also see in Fig. 4A that the propelling velocity depends on the microscopic bending rigidity $\tilde{\kappa}_k$: at low values of k_A (< ~650, pink shaded region in Fig. 4A), the greater the bending rigitidy, the slower the shell swims; at intermediate values of k_A (650~1250, green shaded region in Fig. 4A), either increasing or decreasing bending rigidity from the intermediate value, $\tilde{\kappa}_B = 50\,\epsilon$, would slow down the propulsion; at high values of k_A (> ~1250, blue shaded region in Fig. 4A), the shell with a stronger bending rigidity has faster locomotion. In addition, we notice that the bond strength corresponding to the optimal velocity, $k_{A,m}$, is shifting toward higher values as the bending rigidity $\tilde{\kappa}_A$ increases: $k_{A,m} = 1.0 \times 10^3\ \epsilon/r_c^2$ for $\tilde{\kappa}_A = 10\,\epsilon$, $k_{A,m} = 1.2 \times 10^3\ \epsilon/r_c^2$ for $\tilde{\kappa}_A = 50\,\epsilon$, and $k_{A,m} = 1.3 \times 10^3\ \epsilon/r_c^2$ for $\tilde{\kappa}_A = 90\,\epsilon$. The Föppl-von Kármán (FvK) number[80] (eqn (9)) suggests that $\gamma \propto Y/\kappa$, namely, $\gamma \propto k/\tilde{\kappa}$. The effects of increasing bond strength on the FvK number, therefore, can be offset by increasing the microscopic bending rigidity $\tilde{\kappa}$ and vice versa. Hence, we observe the curves shifting to higher k_A as $\tilde{\kappa}_A$ increases in Fig. 4A. Our results indicate that the propelling velocity of such Janus shells can be controlled and optimized by tuning the mechanical properties of the magnetoelastic membrane.

All the Janus microswimmers in Fig. 4A primarily swim along +y-direction and also exhibit finite unpredictable displacements in x- and z-directions (Fig. S3 in ESI†). Such deviations come from the random rotation of the shells when the magnetic field cannot impose sufficient magnetic torques on the ferromagnetic cap (hemisphere B). In a series of control simulations, we probed the necessity of the permanent dipole moment of the ferromagnetic cap by zeroing the magnetic torque when a misalignment occurs. Our simulation results show that the Janus shells without the magnetic torque starts changing their orientation and sustains spinning after few cycles, resulting in propelling on unpredictable trajectories. Hence, the ferromagnetic cap is essential for maintaining a stable directionality in our design.

3.3 Propelling on a spiral trajectory

So far, we have shown that the microscopic Janus shell is able to swim on a translational trajectory. In the next series of simulations, utilizing a precessing magnetic field (Fig. 5A), we give one example of spiral guidance (Fig. 5B) to demonstrate the feasibility of guiding the Janus shell in desired elaborated trajectories. Here, we take the sample with reference parameters (sample S1, $k_A = 900\ \epsilon/r_c^2$, $k_B = 3000\ \epsilon/r_c^2$, $\tilde{\kappa}_A = 50\,\epsilon$, and $\tilde{\kappa}_B = 50\,\epsilon$) and choose the instantaneous orientation of the dipole moment of the superparamagnetic particles on hemisphere A to be

$$\hat{\boldsymbol{\mu}} = \sin\theta\,\cos\omega t\,\hat{\boldsymbol{\imath}} + \cos\theta\hat{\boldsymbol{\jmath}} + \sin\theta\sin\omega t\,\hat{\boldsymbol{k}}, \qquad (15)$$

and the time dependent field strength is

$$\mu(t) = 1.36(\sin\omega_1 t + 1)/2\,, \qquad (16)$$

which has the same maximum strength as that of the uniaxial field in the previous section. As depicted by Fig. 5A, the field has a precession angle of $\theta = 30°$ around +y-direction and precesses at a frequency of $\omega = 0.5\,\tau^{-1}$ (~1760 s^{-1}). Meanwhile, the magnitude of the field periodically changes at a frequency of $\omega_1 = 2\omega = 1.0\,\tau^{-1}$. The precessing field is

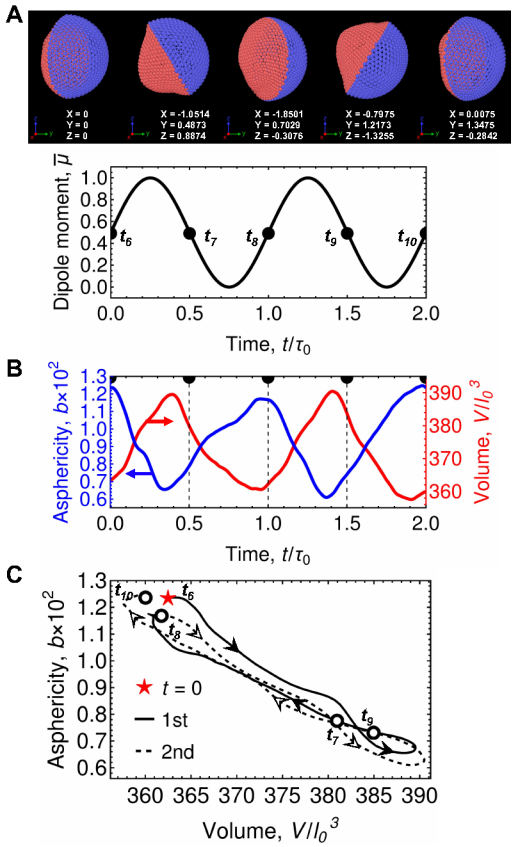

Fig. 6 Dynamics of the Janus shell in one period of the precessing magnetic field as highlighted in the insets of Fig. 5C. (A) Snapshots of the Janus shell at five selected moments, t_6~t_{10} (from left to right, as marked in the time evolution of the normalized dipole moment strength, $\bar{\mu}$). The numbers below each snapshot are the relative displacements in all three directions. (B) Time evolutions of asphericity, b (in blue, left axis) and volume (in red, right axis). (C) The asphericity-volume (b-V) parameter space. The solid and hollow arrows point out the time direction. The paths of first and second halves are indicated by the solid and dashed lines, respectively.

selected in a manner such that the y-component of the intensity remains non-negative in order to avoid flipping the shell's orientation.

Fig. 5C presents the time evolution of displacements corresponding to Fig. 5B. As shown in the insets of Fig. 5C, we find that in one period, the swimmer moves forward twice with one circle turning on the x-z plane. Such motion is expected and consistent with the prescribed pattern of the precessing field: the magnetic field is precessing twice as slow as varying the strength of the dipole moment. Furthermore, we also find that the spiral locomotion generated by the precessing field has an approximate velocity as the translatory propulsion in the uniaxial field, $v = 0.26 \pm 0.06\ r_c/\tau$.

To examine the nonreciprocity of the movement, we focus on the same period as marked in the inset of Fig. 5C and present the snapshots at five selected moments (t_6~t_{10}) in Fig. 6A. The corresponding time evolutions of the asphericity b (in blue, left axis) and the volume enclosed by the shell V (in red, right axis) are shown in Fig. 6B. Comparing with dynamics in the uniaxial magnetic field (Fig. 3B), the precessing field causes the volume to fluctuate within a similar range and a more narrow range for the asphericity. Due to the precessing field, the soft hemisphere A is dragged by the rigid hemisphere B to rotate around the y-axis, leading to a nonaxisymmetric shape observed in hemisphere A (for example, the snapshot at moment t_9). We see in Fig. 6C that the prescribed variations in time possess two cycles with similar areas in the asphericity-volume ($b - V$) parameter space, corresponding to the two forward strokes in each half of the period. It also confirms that the microswimmer undergoes a nonreciprocal motion in such a precessing magnetic field. Our results demonstrate the capability of the Janus swimmer to swim on desired elaborated trajectories by prescribing the temporal pattern of external magnetic fields.

Conclusions

In summary, we designed a magnetically driven microswimmer and demonstrated its feasibility of propelling through viscous fluids in desired complex trajectories. To break the Scallop Theorem, our strategy involves the collaboration between nonreciprocal magnetic fields and build-in asymmetries in both the mechanical and magnetic properties of the two hemispheres. We show that the propelling speed can be optimized by tuning the mechanical properties of the constituent crystalline membrane and explain the mechanisms behind. Though the realization of a system that is identical to our design might be challenging now, the swimming mechanism of our proposed Janus magnetoelastic microswimmer could be applicable to less restrictive systems. For example, a light responsive system can buckle the functionalized part of the Janus shell made of a crosslinked responsive hydrogel. Our study provides a promising template for creating advanced swimmers with enhanced functions and capabilities. We anticipate that future studies will advance the programmable tactic behavior and promote the usage of microswimmers in more specialized tasks. For example, fabricating the crystalline membrane with biodegradable elastic hydrogels may develop a candidate for targeted drug delivery. Energy delivery via multifarious methods also could be realized by adding stimuli-responsive and active materials. Furthermore, fuel-free self-propulsion is possible if self-oscillating chemical reactions are integrated into the system.

Conflicts of interest

There are no conflicts to declare.

Acknowledgements

This work was supported as part of the Center for Bio-Inspired Energy Science, an Energy Frontier Research Center funded by the US Department of Energy, Office of Science, Basic Energy Sciences under Award DE-SC0000989.

Notes and references

1 J. Elgeti, R. G. Winkler and G. Gompper, *Rep. Prog. Phys.*, 2015, **78**.
2 E. Lauga and T. R. Powers, *Rep. Prog. Phys.*, 2009, **72**.
3 Y. Alapan, O. Yasa, B. Yigit, I. C. Yasa, P. Erkoc and M. Sitti, *Annu. Rev. Control. Robot. Auton. Syst.*, 2019, **2**, 205-230.
4 Z. N. Lin, T. Jiang and J. Z. Shang, *Bio-Des Manuf*, 2022, **5**, 107-132.
5 S. Palagi and P. Fischer, *Nat. Rev. Mater.*, 2018, **3**, 113-124.
6 L. Schwarz, M. Medina-Sanchez and O. G. Schmidt, *Appl. Phys. Rev.*, 2017, **4**.
7 Z. G. Wu, Y. Chen, D. Mukasa, O. S. Pak and W. Gao, *Chem. Soc. Rev.*, 2020, **49**, 8088-8112.
8 F. Soto, J. Wang, R. Ahmed and U. Demirci, *Adv. Sci.*, 2020, **7**.
9 J. X. Li, B. E. F. de Avila, W. Gao, L. F. Zhang and J. Wang, *Sci. Robot.*, 2017, **2**.
10 H. Ceylan, I. C. Yasa, U. Kilic, W. Q. Hu and M. Sitti, *Prog. Biomed. Eng.*, 2019, **1**.
11 Z. Chen, X. X. Song, X. L. Mu, J. K. Zhang and U. K. Cheang, *ACS Appl. Mater. Inter.*, 2023, **15**, 8840-8853.
12 C. K. Schmidt, M. Medina-Sanchez, R. J. Edmondson and O. G. Schmidt, *Nat. Commun.*, 2020, **11**.
13 H. T. Chen, Y. Z. Li, Y. J. Wang, P. Ning, Y. J. Shen, X. Y. Wei, Q. S. Feng, Y. L. Liu, Z. G. Li, C. Xu, S. Y. Huang, C. J. Deng, P. Wang and Y. Cheng, *ACS Nano*, 2022, **16**, 6118-6133.
14 J. Wang, Y. Dong, P. Ma, Y. Wang, F. Y. Zhang, B. C. Cai, P. Chen and B. F. Liu, *Adv. Mater.*, 2022, **34**.
15 D. Jang, J. Jeong, H. Song and S. K. Chung, *J. Micromech. Microeng.*, 2019, **29**.
16 N. Dogra, H. Izadi and T. K. Vanderlick, *Sci. Rep.*, 2016, **6**.
17 H. Ceylan, I. C. Yasa, O. Yasa, A. F. Tabak, J. Giltinan and M. Sitti, *ACS Nano*, 2019, **13**, 3353-3362.
18 J. Palacci, S. Sacanna, A. P. Steinberg, D. J. Pine and P. M. Chaikin, *Science*, 2013, **339**, 936-940.
19 D. D. Jin, J. F. Yu, K. Yuan and L. Zhang, *ACS Nano*, 2019, **13**, 5999-6007.
20 M. Urso, M. Ussia and M. Pumera, *Nat. Rev. Bioeng.*, 2023, **1**, 236-251.
21 S. Hermanová and M. Pumera, *ACS Nanosci. Au*, 2022, **2**, 225-232.
22 J. Bastos-Arrieta, A. Revilla-Guarinos, W. E. Uspal and J. Simmchen, *Front. Robot. Ai*, 2018, **5**.
23 Q. L. Zhang, R. F. Dong, Y. F. Wu, W. Gao, Z. H. He and B. Y. Ren, *ACS Appl. Mater. Inter.*, 2017, **9**, 4674-4683.
24 A. C. H. Tsang, E. Demir, Y. Ding and O. S. Pak, *Adv. Intell. Syst.*, 2020, **2**.
25 M. Ilami, H. Bagheri, R. Ahmed, E. O. Skowronek and H. Marvi, *Adv. Mater.*, 2021, **33**.
26 J. J. Abbott, K. E. Peyer, M. C. Lagomarsino, L. Zhang, L. X. Dong, I. K. Kaliakatsos and B. J. Nelson, *Int. J. Robot. Res.*, 2009, **28**, 1434-1447.
27 M. Sitti and D. S. Wiersma, *Adv. Mater.*, 2020, **32**.
28 H. J. Zhou, C. C. Mayorga-Martinez, S. Pane, L. Zhang and M. Pumera, *Chem. Rev.*, 2021, **121**, 4999-5041.
29 K. E. Peyer, L. Zhang and B. J. Nelson, *Nanoscale*, 2013, **5**, 1259-1272.
30 L. D. Yang and L. Zhang, *Annu. Rev. Control. Robot. Auton. Syst.*, 2021, **4**, 509-534.
31 Y. Z. Hou, H. P. Wang, R. X. Fu, X. Wang, J. F. Yu, S. L. Zhang, Q. Huang, Y. Sun and T. Fukuda, *Lab. Chip.*, 2023, **23**, 848-868.
32 L. C. Wang, Z. Y. Meng, Y. Chen and Y. Y. Zheng, *Adv. Intell. Syst.*, 2021, **3**.
33 E. M. Purcell, *Am. J. Phys.*, 1977, **45**, 3-11.
34 E. Lauga, *Soft Matter*, 2011, **7**, 11550-11550.
35 J. W. Swan, J. F. Brady, R. S. Moore and C. 174, *Phys. Fluids*, 2011, **23**.
36 N. Cohen and J. H. Boyle, *Contemp. Phys.*, 2010, **51**, 103-123.
37 T. T. Xu, J. F. Yu, X. H. Yan, H. Choi and L. Zhang, *Micromachines-Basel*, 2015, **6**, 1346-1364.
38 N. Ebrahimi, C. H. Bi, D. J. Cappelleri, G. Ciuti, A. T. Conn, D. Faivre, N. Habibi, A. Hosovsky, V. Iacovacci, I. S. M. Khalil, V. Magdanz, S. Misra, C. Pawashe, R. Rashidifar, P. E. D. Soto-Rodriguez, Z. Fekete and A. Jafari, *Adv. Funct. Mater.*, 2021, **31**.
39 Y. W. Gao, F. N. Wei, Y. Chao and L. G. Yao, *Biomed. Microdevices*, 2021, **23**.
40 H. Shen, S. Cai, Z. Wang, Z. Ge and W. Yang, *Mater. Des.*, 2023, **227**, 111735.
41 S. Nakamura and T. Minamino, *Biomolecules*, 2019, **9**.
42 M. Arroyo, L. Heltai, D. Millan and A. DeSimone, *Proc. Natl. Acad. Sci. U.S.A.*, 2012, **109**, 17874-17879.
43 A. A. Evans, S. E. Spagnolie and E. Lauga, *Soft Matter*, 2010, **6**, 1737-1747.
44 S. V. Nikolov, P. D. Yeh and A. Alexeev, *ACS Macro. Lett.*, 2015, **4**, 84-88.
45C. Wischnewski and J. Kierfeld, *Soft Matter*, 2020, **16**, 7088-7102.
46 C. A. Brisbois and M. O. de la Cruz, *Phys. Rev. Res.*, 2022, **4**.
47 J. Kas and E. Sackmann, *Biophys. J.*, 1991, **60**, 825-844.
48 C. Vanhille-Campos and A. Saric, *Soft Matter*, 2021, **17**, 3798-3806.
49 X. J. Li, *Soft Matter*, 2013, **9**, 11663-11670.
50 X. J. Li, I. V. Pivkin, H. J. Liang and G. E. Karniadakis, *Macromolecules*, 2009, **42**, 3195-3200.
51 P. Colombo, *J. Eur. Ceram. Soc.*, 2008, **28**, 1389-1395.
52 C. I. Zoldesi, C. A. van Walree and A. Imhof, *Langmuir*, 2006, **22**, 4343-4352.
53 J. Jose, M. Kamp, A. van Blaaderen and A. Imhof, *Langmuir*, 2014, **30**, 2385-2393.
54 T. S. Shim, S. H. Kim, C. J. Heo, H. C. Jeon and S. M. Yang, *Angew. Chem. Int. Ed.*, 2012, **51**, 1420-1423.
55 D. Barthes-Biesel, *Annu. Rev. Fluid. Mech.*, 2016, **48**, 25-52.
56 H. Yuan and M. O. de la Cruz, *Phys. Rev. E*, 2019, **100**.
57 F. Quemeneur, C. Quilliet, M. Faivre, A. Viallat and B. Pepin-Donat, *Phys. Rev. Lett.*, 2012, **108**.
58 S. Knoche and J. Kierfeld, *Phys. Rev. E*, 2011, **84**.
59 S. S. Datta, S. H. Kim, J. Paulose, A. Abbaspourrad, D. R. Nelson and D. A. Weitz, *Phys. Rev. Lett.*, 2012, **109**.
60 R. Zandi, D. Reguera, R. F. Bruinsma, W. M. Gelbart and J. Rudnick, *Proc. Natl. Acad. Sci. U.S.A.*, 2004, **101**, 15556-15560.
61 J. Lidmar, L. Mirny and D. R. Nelson, *Phys. Rev. E*, 2003, **68**.
62 G. Vernizzi, R. Sknepnek and M. O. de la Cruz, *Proc. Natl. Acad. Sci. U.S.A.*, 2011, **108**, 4292-4296.
63 S. Y. Li, D. A. Matoz-Fernandez, A. Aggarwal and M. O. de la Cruz, *Proc. Natl. Acad. Sci. U.S.A.*, 2021, **118**.
64 L. Le Nagard, A. T. Brown, A. Dawson, V. A. Martinez, W. C. K. Poon and M. Staykova, *Proc. Natl. Acad. Sci. U.S.A.*, 2022, **119**.
65 S. C. Takatori and A. Sahu, *Phys. Rev. Lett.*, 2020, **124**.
66 M. Paoluzzi, R. Di Leonardo, M. C. Marchetti and L. Angelani, *Sci. Rep.*, 2016, **6**.
67 H. R. Vutukuri, M. Hoore, C. Abaurrea-Velasco, L. van Buren, A. Dutto, T. Auth, D. A. Fedosov, G. Gompper and J. Vermant, *Nature*, 2020, **586**, 52-+.
68 P. J. Hoogerbrugge and J. M. V. A. Koelman, *Europhys. Lett.*, 1992, **19**, 155-160.
69 P. Español and P. Warren, *Europhys. Lett.*, 1995, **30**, 191-196.
70 R. D. Groot and P. B. Warren, *J. Chem. Phys.*, 1997, **107**, 4423-4435.
71 K. P. Santo and A. V. Neimark, *Adv. Colloid Interface Sci.*, 2021, **298**, 102545.
72 P. Espanol and P. B. Warren, *J. Chem. Phys*, 2017, **146**, 150901.
73 S. Plimpton, *J. Comput. Phys.*, 1995, **117**, 1-19.

74 A. P. Thompson, H. M. Aktulga, R. Berger, D. S. Bolintineanu, W. M. Brown, P. S. Crozier, P. J. I. Veld, A. Kohlmeyer, S. G. Moore, T. D. Nguyen, R. Shan, M. J. Stevens, J. Tranchida, C. Trott and S. J. Plimpton, *Comput. Phys. Commun.*, 2022, **271**.
75 A. Stukowski, *Modell. Simul. Mater. Sci. Eng.*, 2010, **18**.
76 D. L. Caspar and A. Klug, *Cold Spring Harb. Symp. Quant. Biol.*, 1962, **27**, 1-24.
77 H. S. Seung and D. R. Nelson, *Phys. Rev. A*, 1988, **38**, 1005-1018.
78 R. Sknepnek, G. Vernizzi and M. O. de la Cruz, *Soft Matter*, 2012, **8**, 636-644.
79 R. M. Erb, J. J. Martin, R. Soheilian, C. Z. Pan and J. R. Barber, *Adv. Funct. Mater.*, 2016, **26**, 3859-3880.
80 A. Libai and J. G. Simmonds, *The Nonlinear Theory of Elastic Shells*, Cambridge University Press, Cambridge, 2 edn., 1998.
81 D. Nelson, T. Piran and S. Weinberg, *Statistical Mechanics of Membranes and Surfaces*, World Scientific Publishing Company, 2004.
82 C. A. Brisbois, M. Tasinkevych, P. Vazquez-Montejo and M. O. de la Cruz, *Proc. Natl. Acad. Sci. U.S.A.*, 2019, **116**, 2500-2505.
83 P. Vazquez-Montejo and M. O. de la Cruz, *Phys. Rev. E*, 2018, **98**.
84 S. E. Spagnolie and E. Lauga, *Phys. Fluids*, 2010, **22**.